

Real-Time Detection of Unmodeled Gravitational-Wave Transients Using Convolutional Neural Networks

Vasileios Skliris, Michael R. K. Norman, and Patrick J. Sutton
*Gravity Exploration Institute, School of Physics and Astronomy,
 Cardiff University, Cardiff, United Kingdom CF24 3AA*

(Dated: October 10, 2022)

Convolutional Neural Networks (CNNs) have demonstrated potential for the real-time analysis of data from gravitational-wave detector networks for the specific case of signals from coalescing compact-object binaries such as black-hole binaries. Unfortunately, CNNs presented to date have required a precise model of the target signal for training. Such CNNs are therefore not applicable to detecting generic gravitational-wave transients from unknown sources, and may be unreliable for anticipated sources such as core-collapse supernovae and long gamma-ray bursts, where unknown physics or computational limitations prevent the development of robust, accurate signal models. We demonstrate for the first time a CNN analysis pipeline with the ability to detect generic signals – those without a precise model – with sensitivity across a wide parameter space. Our CNN has a novel structure that uses not only the network strain data but also the Pearson cross-correlation between detectors to distinguish correlated gravitational-wave signals from uncorrelated noise transients. We demonstrate the efficacy of our CNN using data from the second LIGO-Virgo observing run. We show that it has sensitivity approaching that of the “gold-standard” unmodeled transient searches currently used by LIGO-Virgo, at extremely low (order of 1 second) latency and using only a fraction of the computing power required by existing searches, allowing our models the possibility of true real-time detection of gravitational-wave transients associated with gamma-ray bursts, core-collapse supernovae, and other relativistic astrophysical phenomena.

I. INTRODUCTION

Gravitational-wave (GW) astronomy is now an established field of observational science. To date, the LIGO [1] and VIRGO [2] collaborations have published the details of approximately 90 detection candidates [3–9] over their first three observing runs. The detected signals originate from the binary inspiral and merger of two black holes [10], two neutron stars [11], or one object of each type [12].

Low-latency detection of candidate signals offers arguably the greatest potential scientific payoff, as the GW observations can trigger followup observations in other channels; *i.e.*, multi-messenger astronomy. For example, combined GW and electromagnetic observations of GW170817 - GRB 170817A [13] have yielded novel insights into the origin of heavy elements [14], neutron-star structure [15], GRB astrophysics and host environments [16], and the Hubble constant [17]. Electromagnetic followup of gravitational-wave signals requires very low latency analysis of the GW data - preferably at the second scale to capture the highest energy emissions (e.g., the prompt gamma and x-ray emission of GRBs). Current low-latency GW analysis techniques rely on hundreds of dedicated CPUs and achieve minute-scale latency for automated alerts [18].

Recent work by a number of authors [19–22] has shown that a fundamentally different approach using CNNs has the potential to analyse detector data for GW signals in real time (~ 1 s latency) using a single dedicated GPU. However, most CNNs demonstrated to date require a specific signal model for training (*e.g.* an analytic signal model for binary mergers [19–32], or catalogs of numeri-

cally computed signals for core-collapse supernovae [33–36]), and are therefore only capable of detecting signals matching that model. Many potential sources are governed by physics which is either unknown (*e.g.* the neutron star equation of state [37, 38]) and/or computationally intractable (*e.g.* the modelling of accretion-disk instabilities [39–41]); their transient signals are commonly known as gravitational wave bursts (GWBs). While the unknown physics governing GWBs makes the study of such signals exciting, it also poses a challenge: To fully explore the new GW window we need to be able to detect signals from the widest possible variety of sources without relying on precise models for training.

We address this challenge by proposing a novel CNN architecture that analyses not only the detector strain data directly but also the cross-correlation timeseries between detectors. By training the CNN with ‘featureless’ randomised signals, we are able to construct a neural network that detects coherence (amplitude and phase consistency) between detectors rather than specific signal shapes in individual detectors. We test our resulting analysis pipeline, which we name MLY (“Emily”), using real data from the LIGO-Virgo network and show that it is capable of detecting a variety of simulated GWB signal morphologies without being specifically trained for them, at sensitivities close to that of standard GWB searches, but at much lower latency and a tiny fraction of the computational cost.

This paper is organised as follows. In Section II we give a brief review of applications of machine learning in gravitational-wave astronomy. In section III we present the architecture of MLY’s CNNs and describe the analysis and training procedures. In Section IV we present the

performance of MLy on both simulated and real LIGO-Virgo data. We discuss the implications of these results and next steps in Section V.

II. MACHINE LEARNING IN GRAVITATIONAL-WAVE ASTRONOMY

The fields of gravitational-wave astronomy and deep learning have both advanced significantly in recent years. As such, there has been a confluence of research into their combination and a considerable body of work has developed. Artificial neural networks, including CNNs, autoencoders [42], and various other architectures, have been applied to a variety of problems within gravitational-wave astronomy. In this section we summarise a few of these efforts most closely related to the present work; see for example [43, 44] for wider reviews.

Deep-learning studies in gravitational-wave astronomy have most commonly focused on signals from the inspiral, merger, and ringdown of binaries consisting of black holes and/or neutron stars. A number of groups have demonstrated such methods for the detection of binary merger signals [19–32], as well as for parameter estimation - determining the source properties from a detected signal [23, 27, 28, 45–47]. Deep learning has also been used for fast binary waveform generation [48], which could greatly reduce the time required by traditional Bayesian parameter estimation techniques, and for denoising data around signals [42, 49].

In each of these deep-learning studies, the training of the network has relied on the availability of highly accurate models for gravitational wave signals from binary mergers [50]. The application of deep learning methods to more general types of gravitational-wave signals has been more limited, with core-collapse supernovae being the most prominent example. These studies have made use of either catalogs of gravitational-wave signals from numerical simulations of core collapse or phenomenological waveform models fit to such catalogs. For example, Chan *et al.* [33] trained a CNN using simulated gravitational-wave timeseries with core collapse supernovae signals drawn from a range of published catalogs covering both magnetorotational-driven and neutrino-driven supernovae, and measured the ability to both detect the signal and correctly classify the type. Iess *et al.* [34] considered the problem of distinguishing true signals from noise fluctuations (“glitches”) that are common in real detectors. They used signals drawn from numerical catalogs combined with a simple phenomenological models for two glitch types to train CNNs to distinguish supernova signals from noise glitches. Lopez *et al.* [36] (building on [35]) used a phenomenological model mimicking gravitational-wave signals from non-rotating core-collapse supernovae to train a complex mini-inception resnet neural network [51] to detect supernova signals in time-frequency images of LIGO-Virgo data.

We note that all of these examples, both for binary mergers and for supernovae, rely on having a signal model to train the deep network. As a consequence, their applicability is restricted to signals that are similar to the training data. While not an issue for binary mergers, this may be very important for supernovae where the simulations used for training rely on uncertain physics and numerical approximations and simplifications [52, 53]. And they are clearly not applicable to the more general problem of detecting gravitational-wave transients from as-yet unknown sources.

Shortly after the release of an early version of this work [54], Marianer *et al.* [55] presented a deep-learning algorithm that avoids relying on a signal model by instead using outlier detection. The authors trained a mini-inception resnet network [51] on the Gravity Spy data set [56, 57], which contains spectrograms of known noise glitches classified into categories. They then applied the CNN to spectrograms of LIGO data and used two methods of outlier detection to identify possible signals. This search was applied to a subset of public LIGO data from the first two observing runs; no signal candidates were found. To our knowledge this is the only other case to date of a deep-learning method capable of searching for generic gravitational-wave transients.

In this paper we present a deep-learning technique that is capable of detecting generic transient gravitational-wave signals. Our approach differs from previous approaches in a key way: rather than training a CNN to recognise specific signal morphologies in the data streams, we construct CNNs that are designed to recognise *coherence* in amplitude and phase between two or more data streams. We then train the CNNs using simulated signals and noise glitches that both consist of *random* timeseries with properties drawn from the same distributions. Using the same waveform distributions to simulate both the signals and glitches prevents the CNNs from using the signal morphology to the classify input. Instead, the CNNs are forced to learn to measure consistency between detectors.

In the next section we describe the architecture of MLy’s CNNs and the training procedure. We then evaluate MLy by analysing data from the second LIGO-Virgo observing run. We will see that our trained pipeline has a detection efficiency approaching that of the standard LIGO-Virgo pipeline for detecting unmodelled gravitational-wave transients [58], but with much higher speed and much lower computational cost.

III. A CNN FOR UNMODELLED BURST DETECTION

A. Network Architecture

Our goal is to be able to detect sub-second-duration GWBs in data from the three detectors of the LIGO-Virgo network, without prior knowledge of the signal

morphology. A significant challenge is to distinguish real signals from the background noise transients, “glitches”, that are common in these detectors [59–61]. Typical GWB detection algorithms [62–65] do this by requiring candidate signals to be seen simultaneously in multiple detectors (simultaneously up to the light travel time between the detectors) and to be correlated between detectors. We follow this logic in our analysis by using a network architecture for ML_y that combines the outputs of two different CNNs: one that detects coincident signals in multiple detectors (Coincidence Model - Model 1), and a second that detects correlation in phase and amplitude between the detectors (Coherence Model - Model 2).

1. Coincidence Model - Model 1

The first model is a single-input single-output residual neural network whose main goal is to identify real signals from noise. More specifically it tries to identify coincident signals that appear in at least two detectors. This model takes as input the whitened timeseries data from each of the three LIGO-Virgo detectors. The output is a score on $[0, 1]$, where high values indicate signal and low values no signal.

Residual neural networks are proven to boost the performance of simpler CNNs by reducing the effect of vanishing gradients; the latter make deep CNNs lose contributions from their first layers and cause their efficiency to saturate. We adapt a network from [66] that compares different methods of using machine learning on time-series data and we optimise it using a genetic algorithm (see below). We find that the resulting residual neural networks outperforms “ordinary” deep CNNs in our case. More specifically we optimise a simple CNN model with a relatively good performance (overall accuracy $>95\%$) and then use it as a “residual block”, where we feed the output of the block to its input. To find the hyper-parameters of the model we use a genetic algorithm that trains many generations of different randomly initialised models and find which hyper-parameters increase the performance. The two main differences from the original model of [66] are a larger kernel size and the reduction in our residual blocks from three layers to two. We find that three residual blocks are optimal, as in [66]. Varying the number of filters has no obvious benefit so we retain the original number to make the model less computationally expensive. The final modification is the use of a cyclical learning rate [67] that boosts the performance by 2%.

The final model is shown in Figure 1. It has three residual blocks, the first with 64 filters and the others with 128. At the end of each residual block we add output of the first layer to the block output. By doing this the gradient can skip the intermediate layer reducing the vanishing effect. Since we use convolution, all layers are zero-padded to maintain the same size with the input and make this addition feasible. At the end of each layer

we apply ReLU (rectified linear unit) activation followed by batch-normalisation. After the last residual block we flatten using global average pooling. We then use two dense (fully connected) layers with batch-normalisation before passing to the output layer, which uses sigmoid activation. We use binary cross entropy to calculate the loss.

We discuss the training of this model in Section III C.

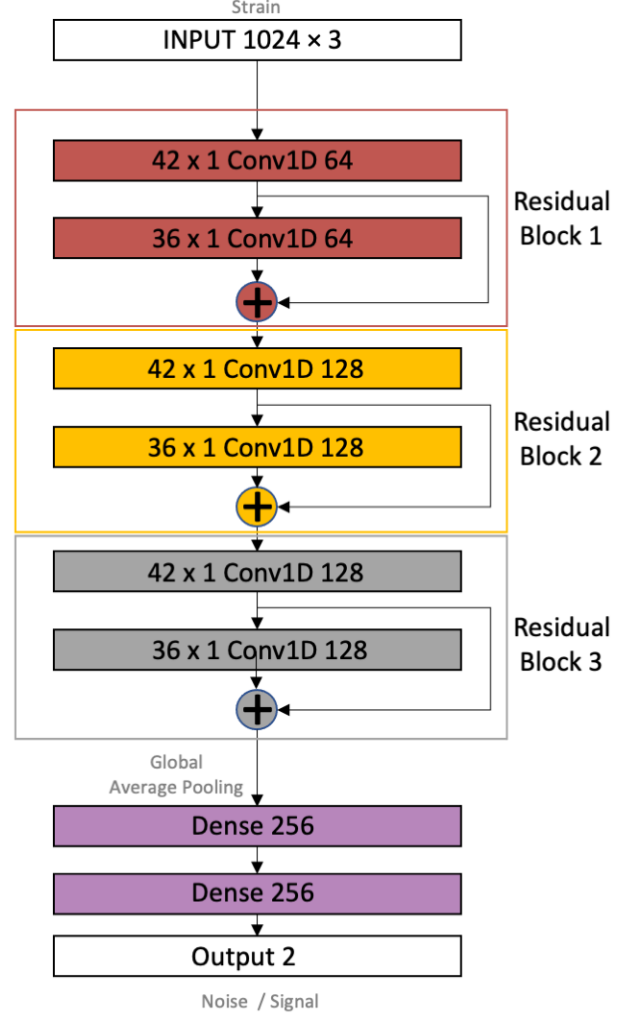


Figure 1. Coincidence model architecture (Model 1). The input consists of 1024-sample whitened data streams from the H, L, and V detectors. This is passed through three consecutive two-layer residual blocks, flattened, then passed through two final dense layers. $M \times N$ indicates the size of the filters in each convolutional layer and 64/128/256 is the number of filters (convolutional layers) or nodes (dense layers).

2. Coherency Model - Model 2

The second model has two inputs and one output. The first input is the same whitened timeseries data fed to the first model, while the second input is the Pearson

correlation of each pair of detectors:

$$r_{\alpha\beta}[n] = \frac{\sum_{i=1}^N (d_{\alpha}[i] - \bar{d}_{\alpha})(d_{\beta}[i+n] - \bar{d}_{\beta})}{\sqrt{\sum_{j=1}^N (d_{\alpha}[j] - \bar{d}_{\alpha})^2 \sum_{k=1}^N (d_{\beta}[k] - \bar{d}_{\beta})^2}}. \quad (1)$$

Here $d_{\alpha}[i]$ is the whitened data timeseries for detector α , \bar{d}_{α} is the mean over N samples, and n is an integer time delay between detectors. The correlation is computed for all n corresponding to time delays of up to ± 30 ms with respect to the first detector, which is slightly larger than the maximum possible arrival time difference (± 27.3 ms) a GW signal can have in the HLV network.

Measurements of correlation between detectors have long been a key ingredient of GWB detection pipelines; see *e.g.* [58, 64, 68–70]. We have explored training networks to infer correlation information from the strain data; however, this is not a natural operation for networks constructed from convolutional filters. Since the Pearson correlation is simple to compute and easy to digest by a feature-detecting algorithm, we choose to feed the correlation as an input to the model.

The strain and correlation inputs have their own separate branches which are eventually merged as shown in Figure 2. Like the first model, we use a genetic algorithm to optimise the hyper-parameters. Due to the small size of the correlation input, we find that its branch does not need to be as deep as the coincidence model, nor does the strain branch. We find that the performance is sensitive to the number of filters: increasing or decreasing the number in any of the convolutional layers can prevent the model from training. By contrast the kernel size has no significant effect on performance, except for some variation of the stability of training in some cases. The choice of kernel size was made based on how often those numbers appeared in the gene pool of the last generation of successful models in the genetic algorithm.

The final model is shown in Figure 2. We pass the strain input through three convolutional layers and the correlation data through two convolutional layers in a separate branch. (We also explored residual neural networks for the strain branch of the model but these gave no improvement in performance.) We flatten the outputs by global average pooling, which increases the performance slightly, and then combine the two branches with concatenation before passing through a dense layer.

This model has a binary classification output that is trained to return a measure of coherency among detectors on $[0,1]$. We discuss the training of this model in Section III C.

B. Analysis Procedure

We analyse data from all three of the detectors in the LIGO-Virgo network: LIGO-Hanford (H), LIGO-Livingston (L), and Virgo (V). In our analysis we use two types of background noise. For testing we use real

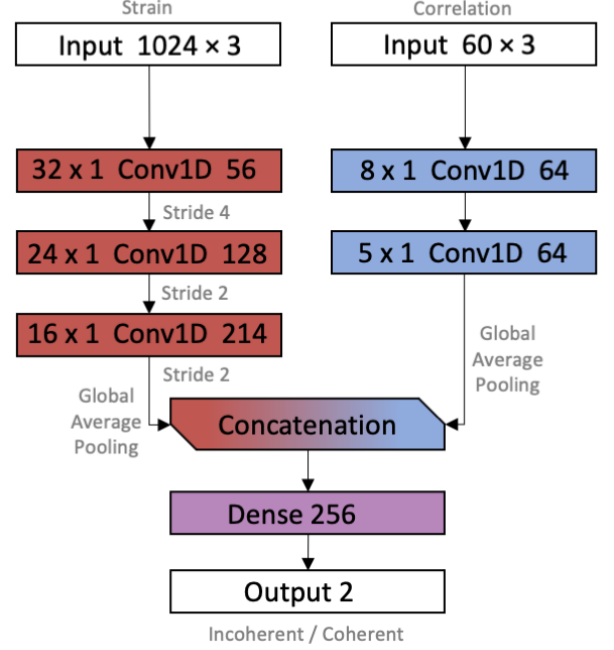


Figure 2. Coherence model architecture (Model 2). The model consists of two branches with separate inputs. The input of the left branch consists of the same 1024-sample whitened data streams as input to Model 1 (Figure 1). This is passed through three consecutive convolutional layers, flattened, then passed through two final dense layers. $M \times N$ indicates the size of the filters in each convolutional layer and 64/128/256 is the number of filters (convolutional layers) or nodes (dense layers).

LIGO-Virgo data publicly available from the GW Open Science Center (GWOSC) [71]. For training we use simulated Gaussian noise that follows the design curves for the LIGO and Virgo detectors [72]; the motivation for using simulated noise for training is explained in Section III C.

The LIGO-Virgo data from GWOSC are sampled at 4096 Hz. We downsample to 1024 Hz, allowing us to detect signals up to 512 Hz; this covers the most sensitive frequency range of the detectors and is sufficient for the purpose of demonstrating our CNN. (Since the trained network can process data much faster than real time, we could extend the analysis to higher sample rates. We leave this to future work.) We chose to focus on signal durations < 1 s by analysing data in 1 s segments. This covers many plausible signal models, including for example core collapse supernovae [73], perturbed neutron stars and black holes [12], and cosmic string cusps [74]. We could extend to longer durations as well, with a corresponding increase in latency.

The power spectral density $S_{\alpha}(f)$ for each detector α is computed using Welch’s method, and used to whiten the corresponding data stream. Each data stream is also high-pass filtered at 20 Hz, giving a search band of $[20, 512]$ Hz. At our chosen sampling rate this means that the timeseries data is fed to the CNN in an array of size

[1024×3]. The Pearson correlation is computed between each pair of bandpassed whitened data streams for time delays in steps of one sample over ± 30 ms, for a total of 60 samples; this data is therefore in an array of size [60×3].

The bandpassed whitened data series and the correlation series are then fed into the two models. The scores from the two models are multiplied together to give a combined score on [0, 1]. In this way a candidate signal needs to score highly for both models; *i.e.*, showing both coincidence in multiple detectors and correlation between the detectors. In practice we find the scores of both models tend to be strongly peaked around 0 for noise and weak signals, and strongly peaked around 1 for strong signals.

To estimate the distribution of scores of the background noise, we repeat the analysis many times after time-shifting the data between detectors by an integer number of seconds. Since the time shift is much larger than the largest possible time-of-light delay between detectors, it prevents a real GW signal from appearing in coincidence between multiple detectors. All coincident events in the time-shifted series can therefore be assumed to be uncorrelated and treated as background noise. This is a standard procedure in GW analysis; see *e.g.* [59].

To estimate the sensitivity to GWBs, we repeat the analysis after adding simulated signals to the data. In General Relativity, a GW has two polarisations, denoted $h_+(t)$ and $h_\times(t)$. The received signal $h_\alpha(t)$ of a given detector α is the combination

$$h_\alpha(t) = F_\alpha^+ h_+(t) + F_\alpha^\times h_\times(t) \quad (2)$$

where the antenna response functions $F_\alpha^{+,\times}$ are determined by the position and orientation of the source relative to the detector. We characterise the strength of the received signal by its network signal-to-noise ratio

$$\rho = \sqrt{\sum_\alpha 4 \int_0^\infty \frac{|\tilde{h}_\alpha(f)|^2}{S_\alpha(f)} df}. \quad (3)$$

Generating simulated signals distributed isotropically over the sky and rescaling to different ρ values allows us to measure the distribution of CNN scores as a function of the signal-to-noise ratio of the signal.

C. Training

The choice of data used to train a CNN is often a critical factor for the CNN’s performance.

For the signal population we use white-noise bursts (WNBs) [59, 64]; these are signals where the h_+ and h_\times polarisations are independent timeseries of Gaussian noise that is white over a specified frequency range, multiplied by a sigmoid envelope. We select these as our training sample as they are effectively featureless.

The bandwidth of each simulated (or “injected”) signal is selected randomly and uniformly over the range [40, 480] Hz. The duration of each injection is selected randomly and uniformly over the range [0.05, 0.9] s. Given their duration their central time is chosen randomly inside this 1-second interval in a way that they don’t get cropped. The injections are distributed uniformly over the sky and projected onto the detectors using equation (2). Finally, the signal is rescaled to a desired network signal-to-noise ratio ρ as defined in equation (3). In the rest of this section we will discuss different aspects of our training data and methods, that eventually gave us the current best model.

For the background population we find in practice that the best CNN performance is obtained by training with *simulated* detector noise and glitches, rather than real glitching detector noise. The simulated glitches are WNBs with parameters drawn from the same distribution as for GWBs, but independently between detectors (*i.e.*, a different WNB is used for each detector). Using simulated background allows us to control the glitch rate in the training set; we will show in Section III C 3 that we can vary this rate to reduce the false alarm rate of the trained models and maximise their performance. Furthermore, using WNBs for the glitches prevents the CNNs from learning to distinguish GWBs from glitches based on the morphology; this is critical since we do not know the true morphology of GWBs.

In the remainder of this section we detail the training process for each model. All training data were generated using the MLY-pipeline package [75] and its generator function, with elements of the PYCBC [76] and GWPY[77] package to project the signal onto the detectors and apply time-of-flight differences to the signals arriving at the various detector locations. For training the models we used KERAS [78]. More details and the codes are available at our repository [79].

1. Data types

We have two CNN models to train: the Coincidence Model (model 1) and the Coherence Model (model 2). Each model is trained with a dataset chosen to produce the best performance of the model for its assigned task.

All training samples consist of stationary background noise and optionally an injection into one of more of the detectors. The stationary background is Gaussian noise with power spectra that follow the design curves of the LIGO and Virgo detectors [72]. For the non-stationary glitch component we use the same WNB waveform family as for the GWB signals but either do the injection into a single randomly chosen detector or we inject into all three detectors but select the WNB parameters independently for each detector. We use a total of four types of samples:

- **Type 1:** Gaussian LIGO-Virgo noise, with no injections. Labeled as noise.

- **Type 2:** Gaussian LIGO-Virgo noise with coherent WNB injections in all detectors, simulating a real GWB. Labeled as signal.
- **Type 3:** Gaussian LIGO-Virgo noise with different (incoherent) WNB injections in each detector, simulating unrelated glitches or excess noise in each detector. The injections may be simultaneous or offset in time from each other to simulate simultaneous or nearly simultaneous glitches. Labeled as noise.
- **Type 4:** Gaussian LIGO-Virgo noise with a single WNB injection in a randomly chosen detector, simulating a glitch in a single detector. Labeled as noise.

The Coincidence Model (model 1) is trained using Type 1 (stationary background), Type 2 (GWBs), and Type 4 (single-detector glitches). The GWBs are injected with network SNR values in the range [12,30]. The limits of this range are chosen based on the fact that lower SNR values in training increase the false alarm rates dramatically, while training SNRs higher than 30 are not required; we show later that the detection efficiency remains high for SNR values larger than those in the training set. Single-detector glitches (Type 4) have SNR values over the range [6,70].

The Coherence Model (model 2) is trained using Type 1 (stationary background), Type 2 (GWBs), and Type 3 (incoherent multi-detector glitches). Experimentation showed that training with GWB network SNRs in the range [10,50] and glitch network SNRs in the range [10,70] gives the best performance.

The Type 3 incoherent signals represent the extreme cases where glitches are present in the same 1-second interval in all three detectors. Real glitches occur independently in different detectors and need not be simultaneous to within the light travel time between detectors. To train our model to handle this case we define a quantity called “disposition” which is the range of central times of the glitches. For example, in the case of three detectors and a disposition T seconds the glitches will be centred at times $T_0 - T/2$, T_0 , and $T_0 + T/2$ seconds in the three detectors, with the order selected randomly. The central time T_0 is positioned randomly in the 1 second interval so that no signal gets cropped, and the injection durations are also restricted so that no signal gets cropped. We generate datasets for dispositions distributed uniformly over three different ranges: Type 3a has range of [0.1,0.5] seconds, Type 3b has range [0,0.1] seconds, and Type 3c has zero disposition to challenge the Coherence Model with coincident incoherent signals.

2. Reproducibility

It is crucial for a method or model to have reproducible results if it is going to be compared with another. Machine learning models typically use random initialisation

of their trainable parameters, which can lead to different results for repeated runs of the training. As a demonstration of this effect, we train each of models 1 and 2 ten times each, yielding 100 combinations of trained models. Figure 3 shows the distribution of background scores for each trained version of each model separately and for all 100 model 1 – model 2 pairs. We see that while the performance of each model is variable between trainings, the average performance curves are much smoother and more regular. In the following sections we follow this practice of averaging over repeated trainings of the same model to make more robust comparisons of different methods of training.

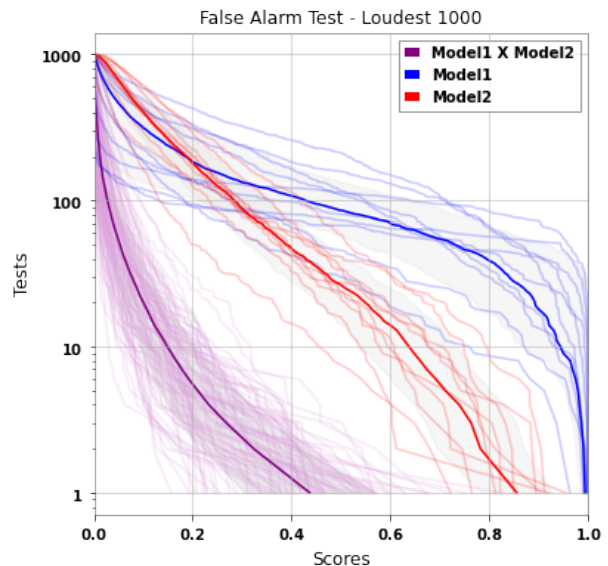


Figure 3. False alarm test results for 10 different trainings of model 1 (blue) and model 2 (red) and their 100 combinations (magenta) of scores. The same 1 month of background noise data was used for testing each trained model. We present here the distribution of the 1000 highest background scores for each model. We highlight with a bold line the mean result for each model. The gray area represent one standard deviation for each case.

3. Training sample ratios

In classification problems the training data often contain the same number of examples in each class, giving all classes equal importance. In our problem we prioritise the reduction of false alarms (false positives) and the ability of the network to recognise noise. This is motivated by the low false alarm rate threshold adopted by LIGO and Virgo for issuing GWB detection alerts during online running, currently 7.9×10^{-9} Hz (one per 4 years) [80]. Even with our best model, using equal numbers of signal and noise samples gives a false alarm rate of $\sim 1/\text{day}$. Furthermore we have more than just stationary noise and GWB injections in our data types: we also

try to simulate single- and multi-detector glitches, so we need to investigate the optimal proportions of each type. We therefore trained both models with different ratios of the data types to determine which proportions provide the best performance.

For the Coincidence Model (model 1) we tested all combinations of $3N$ and $6N$ instances each of Type 1 and Type 2, and $3N$, $6N$, and $12N$ instances of Type 4, where $N = 10^4$, for a total of 12 different combinations. For the Coherence Model (model 2) we tested all combinations of $5N$ and $10N$ instances each of Type 1, Type 2, Type 3a & b together, and Type 3c, for a total of 16 different combinations. For each combination we repeat the training 7 times and use the mean false alarm curve and detection efficiency for comparisons. We get in total $12 \times 16 = 192$ different combinations of models 1 & 2.

As described in more detail in section IV, the ranking of a model is defined by the minimum SNR at which it achieves 50% detection efficiency at a fixed false alarm rate. After training, the detection efficiency and false alarm distribution for each model combination was evaluated using a common set of real background noise data from the second LIGO-Virgo observing run (O2 [60], August 2017) and a common set of GWB injections. We find the best performance results from training model 1 with Types 1, 2, 4 in the amounts $3N$, $3N$, $6N$ and training model 2 with Types 1, 2, 3a&b, 3c in the amounts $5N$, $5N$, $10N$, $5N$. It is interesting to see that in both cases the best training requires many more glitch-like samples than stationary noise or signal samples. That supports our assertion that varying the proportion of glitches in the training sample can be used to improve performance.

4. Rescaled Virgo noise level

In the previous section we varied the proportion of simulated glitches in the training set to maximise performance. We can perform a similar experiment with the level of the stationary background noise component. Up to this point we have trained with artificial Gaussian noise that follows the design noise power spectral density of the advanced LIGO and Virgo detectors [72]. When considering the O2 data, we note that the ratio of the noise level in Virgo to that in the LIGO detectors is higher than the ratio for the design noise spectra. This means that in the real data we expect the SNR of a signal in Virgo relative to LIGO to be systematically lower than the SNR used in training, potentially resulting in sub-optimal model performance on real data. To investigate this we retrain the best model from the previous investigation (Section III C 3) after rescaling the Virgo background by the factors 0.5, 1, 2, 4, 8, 16, or 32. Rescaling by 1 is the same training as before, while the factor of 0.5 is for a sanity check on the method. All other factors (> 1) lower the SNR of the training signals in Virgo relative to LIGO. For each case we repeat the training 7 times and use the mean to compare the

different rescalings.

Figure 4 shows that higher rescaling lowers the typical false alarm rate for a given output score (with some fluctuation in the scores of the very loudest events due to small-number statistics). We find that the output score of simulated GWBs does not vary significantly with the Virgo rescaling; since the false alarm rate is lower, this leads to an overall improvement of detection efficiency for a given false alarm rate. This is demonstrated in Figure 5, where we see that Virgo rescalings of $\gtrsim 10$ maximise the overall detection probability for a population of WNB GWBs distributed isotropically over the sky. We therefore select a rescaling factor of 32 as the optimal choice.

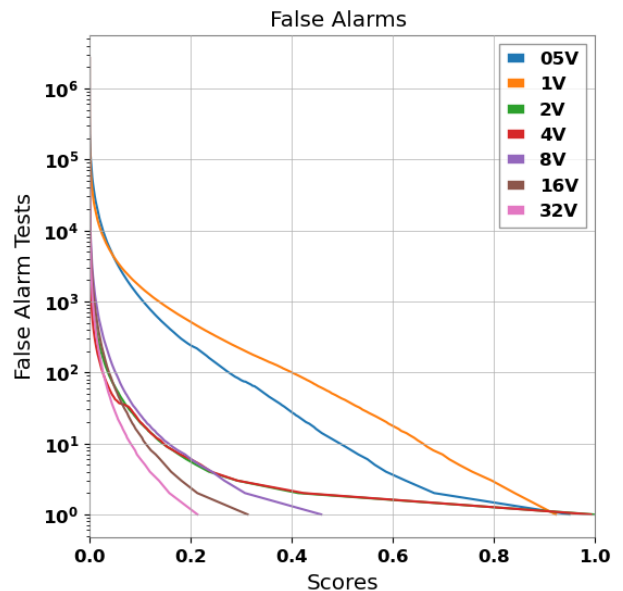


Figure 4. Average false alarm distributions out of 49 different combinations of model 1 and model 2 for different rescalings of the Virgo background noise. Exactly 1 month of time-lagged data was analysed.

Rescaling the Virgo noise level upwards lowers the SNR of signals in Virgo used for training, causing the models to learn to put less emphasis on the Virgo data. One might question whether this large rescaling means that the Virgo data is no longer useful. As a test, we performed a series of injections where each injection was done twice: once normally, with the signal added to all three detector data streams; and again where the same injections were made into Hanford and Livingston but no signal was added to the Virgo data stream. We find that while the scores for most injections are largely unchanged, zeroing out the Virgo injection lowers the scores significantly in some cases, particularly for high SNR signals. This demonstrates that even with the elevation of the Virgo noise for training, the models can still extract useful information from the Virgo data stream.

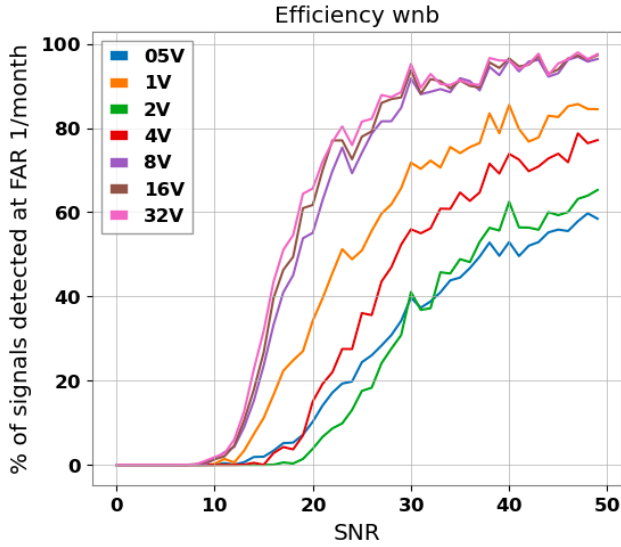


Figure 5. Average efficiencies out of 49 different combinations of model 1 and model 2 for different rescalings of the Virgo background noise. The GWB signals are WNBs distributed isotropically over the sky. The efficiency is evaluated at a false alarm rate of 1 per month, which corresponds to the loudest event on each curve in Figure 4

IV. PERFORMANCE

Following our investigations into optimising the training procedure, we now evaluate the performance of MLY's optimally trained models on real LIGO-Virgo data. For these tests we use models trained with the optimal training sample ratios (Section III C 3) and with the Virgo noise rescaled by a factor of 32 above its design level (Section III C 4). Of the 49 combinations of model 1 and model 2 that were trained in this way, we select the one that has the best performance based on tests with real LIGO-Virgo data.

A. False Alarm Rate

A standard means to assess the performance of a GWB detection algorithm (see *e.g.* [59]) is to measure the detection efficiency for various signal morphologies as a function of the signal amplitude (*e.g.*, signal-to-noise ratio) at a fixed false alarm rate.

We calculate the false alarm rate (FAR) as a function of score by analysing background data samples that are independent from those used in the training. For the final models we measure the FAR using real LIGO-Virgo data from the second observing run [60] during times when all three detectors were operating (1 - 25 Aug 2017), with time shifts applied as discussed in Section III B.

Figure 6 shows the FAR versus output score for real LIGO-Virgo data. For comparison, we also show the FAR for simulated Gaussian noise; we see that the FAR of our

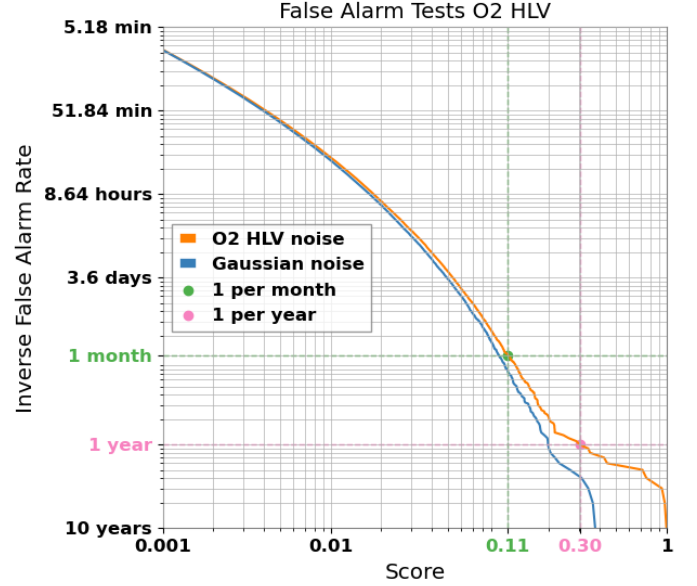


Figure 6. The false alarm rate of MLY's combined optimised models on real O2 noise in comparison with the false alarm rate on Gaussian noise. The score thresholds of 0.11 and 0.30 correspond to false alarm rates of 1/month and 1/year on real noise.

combined models on real data is very similar to that on ideal Gaussian noise down to false alarm rates of a few per year. For FARs 1/year or lower there is a tail of high-scoring background events in the real data that requires setting a higher score threshold than needed for Gaussian noise, meaning our combined model sensitivity on real data is lower than the idea case at those low rates.

For comparisons to other GWB detection methods, we choose to compute our detection efficiencies at a FAR threshold of 1/year. This threshold is motivated by being similar to the LIGO-Virgo FAR threshold for issuing public alerts of candidate GW signals [80].

B. Detection Efficiency

We calculate MLY's detection efficiency for a selection of different possible GWB signals, both for the case of simulated Gaussian background noise and for real LIGO-Virgo data from the second observing run. In each case we generate new sets of signal injections (different from the training data) and add them on to simulated noise or noise randomly sampled from the O2 observing run during times when all three detectors were operating. We measure our sensitivity to five distinct waveform morphologies:

WNB: These are the same type of signal as the Type II used for training.

CSG: A circularly polarised sinusoidal signal with Gaussian envelope. These *ad hoc* waveforms are stan-

dard for testing GWB analyses [59, 60].

CCSN: The N20-2 waveform of [81], from a 3D simulation of a neutrino-driven core-collapse supernova (CCSN) explosion.

Cusp: The GW emission expected from cosmic string cusps [82].

BBH: The GW signal from a black-hole binary merger. We used the IMRPhenomD waveform model [83, 84]. The black-hole masses and spins were selected randomly and uniformly over the intervals $[10, 100] M_\odot$ and $[-1, 1]$, with the restriction that the maximum signal frequency does not exceed 512 Hz.

Sample waveforms of each type are shown in Figure 7.

We compute the efficiencies at SNR values $\rho = 0, 1, 2, \dots, 50$, where the $\rho = 0$ case corresponds to pure noise (where we expect approximately zero efficiency). For each SNR value we generate 10^3 injections. Each injection is rescaled to the desired network SNR, added to the background timeseries, and processed by the models giving a score. The injection is considered to be detected if the combined output score is larger than that of the false alarm rate threshold.

Figure 8 shows the detection efficiency for each case. We see that MLY is able to detect $>50\%$ ($>90\%$) of all signals that have amplitudes $\rho \geq 19$ ($\rho \geq 27$), with the exception of cusps for which the sensitivity is lower. The performance for CCSN and BBH signals is very similar to that for WNBs, even though the signal morphologies are quite different (see Figure 7). The performance for CSGs is even better, which we attribute to the very small time-frequency volume that it occupies making the signal louder. The performance for cusps is poorer; tests indicate that this occurs because cusps are linearly polarised ($h_\times = 0$) while the WNB training injections are unpolarised polarised ($|h_\times| = |h_+|$). In the next subsection we will see a similar effect for linearly polarised sine-Gaussian signals. This is an interesting demonstration of where our training could potentially be improved to handle a yet broader range of signals.

Three real BBH events were reported by LIGO and Virgo during O2 while all three of the detectors were operating: GW170809 (SNR ~ 12), GW170814 (SNR $\lesssim 17$), and GW170818 (SNR ~ 11) [3]. None were detected by MLY. This is not surprising; comparing the reported SNRs to Figure 8, we estimate that the loudest event, GW170814, has a probability of being detectable of less than ~ 0.24 , while the other two events have SNRs that are too low to be detectable by our analysis.

C. Comparison with the LIGO-Virgo all-sky search in O2

The LIGO-Virgo collaborations have already searched the O2 data looking for generic short-duration GWB sig-

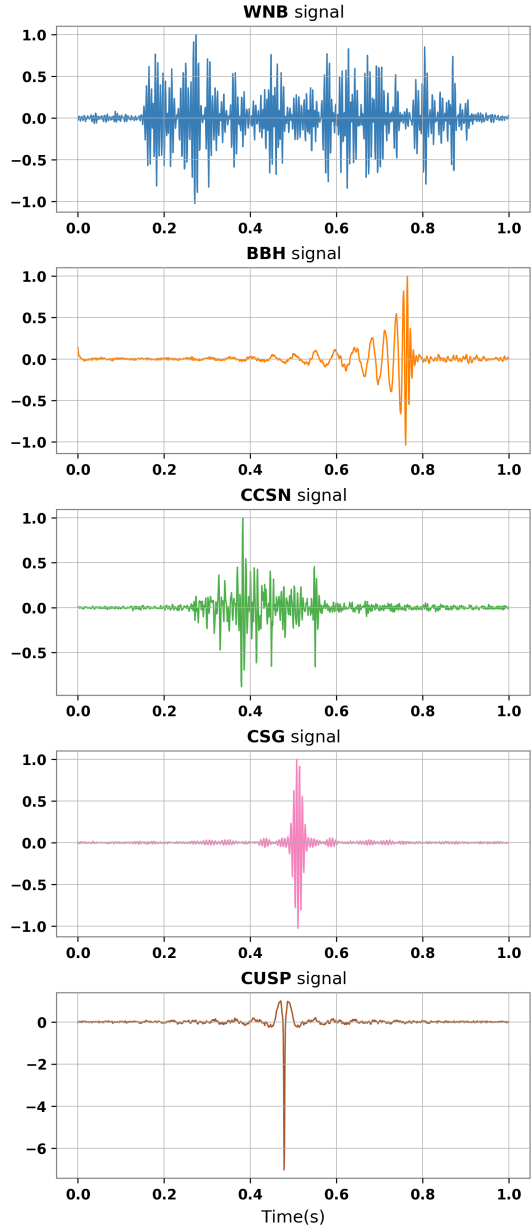


Figure 7. Examples of testing signals: white noise burst (WNB), binary black hole merger (BBH), core-collapse supernova (CCSN), circularly polarised sine-Gaussian (CSG) and cosmic string cusp. All plots show the injection after whitening, but without background noise.

nals [60]. We compare the performance of MLY with that

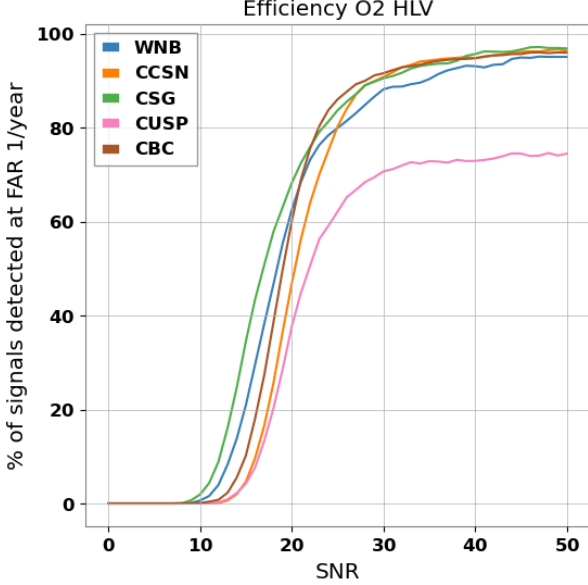


Figure 8. Detection efficiency: the fraction of simulated signals that are detected at a false alarm rate of 1/year versus the network SNR defined by equation (3). The waveform morphologies are white noise burst (WNB), core-collapse supernova (CCSN), circularly polarised sine-Gaussian (CSG), cosmic string cusp, and binary black hole merger (BBH).

of the LIGO-Virgo analysis by repeating the signal injections performed in the LIGO-Virgo search for all signal types reported in [60] with maximum frequencies below 500 Hz; these signal types are listed in Table I and consist of Gaussian pulses, sine-Gaussians, and WNBs (see [60] for details).

The procedure to assess efficiencies is the same as that used in previous sections except that, following LIGO-Virgo convention, instead of using SNR the injected signal strength is characterised by the root-sum-square value h_{rss} :

$$h_{\text{rss}} = \sqrt{\int_{-\infty}^{\infty} dt (|h_+(t)|^2 + |h_{\times}(t)|^2)} \quad (4)$$

(Note that the h_{rss} calculation is independent of the detectors or their noise spectra. Hence for a given h_{rss} , signals at frequencies of higher detector noise will have a lower SNR. There is therefore no one-to-one match between SNR and h_{rss} .)

Figure 9 shows the detection efficiency of MLy for the tested waveforms, at a FAR threshold of 1/year. We see a pattern similar to Figure 8: most waveforms have similar efficiencies, with two having poorer performance. The two poorly performing waveforms, G2D5 and SGL1538D9, are the only linearly polarised waveforms in the set. This is very similar to the behaviour of the linearly polarised cosmic string cusp waveforms in

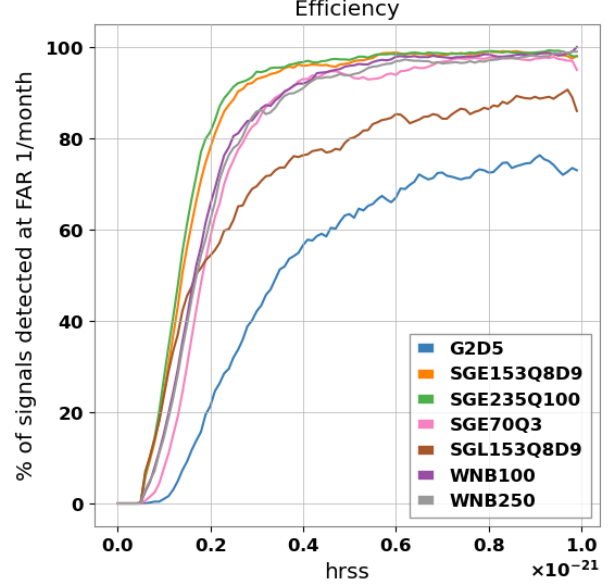


Figure 9. The detection efficiency of the MLy pipeline as a function of the h_{rss} amplitude for the burst signal types listed in Table I. The efficiency is computed at a false alarm rate threshold of 1/year.

Figure 8, and supports the notion that the lower performance is due to training with exclusively unpolarised waveforms.

Table I reports the h_{rss} values at which MLy achieves a detection efficiency of 50% for each waveform. It also shows the h_{rss} values at which CWB achieves a detection efficiency of 50% [85]. We see that MLy's h_{rss} limits are approximately 10% to 50% higher than for CWB, corresponding to sensitivity to distances that are 65% to 90% as far as those of CWB. We consider this to be a very promising first demonstration of the power of machine learning for GWB detection, particularly when one considers the very low computational cost and high speed of the MLy analysis (discussed next).

D. Inference and Training Times

We note that the CNN analysis of data is very fast: we find that the average time required to process 1 second of whitened data is 51 ms on a 3.5 GHz Xeon E3-1240v5 quad-core CPU with 32 GB of RAM, or approximately 3.3 ms on a A100-SXM4-80GB GPU. This makes second-scale-latency searches feasible, much faster than the minute-scale latency typical of current LIGO-Virgo low-latency searches [18].

The overall computational cost is also very low compared to traditional search algorithms. The dominant computational cost of our analysis is in estimating the FAR. Approximately 10^3 time shifts is enough

Name	+/ \times	Parameters	cWB	MLy ($10^{-22} \text{ Hz}^{-1/2}$)
<i>Gaussian pulses</i>				
G2D5	L	$t=2.5 \text{ ms}$	2.8	3.5
<i>Sine-Gaussian pulses</i>				
SGE70Q3	E	$f_0=70 \text{ Hz}$, $Q=3$	1.5	1.9
SGE153Q8D9	E	$f_0=153 \text{ Hz}$, $Q=8.9$	1.3	1.4
SGL153Q8D9	L	$f_0=153 \text{ Hz}$, $Q=8.9$	–	1.7
SGE235Q100	E	$f_0=235 \text{ Hz}$, $Q=100$	0.9	1.4
<i>White-Noise Bursts</i>				
WNB100	U	$f_{\text{low}}=100 \text{ Hz}$, $\Delta f=100 \text{ Hz}$, $t=0.1 \text{ s}$	1.2	1.7
WNB250	U	$f_{\text{low}}=250 \text{ Hz}$, $\Delta f=100 \text{ Hz}$, $t=0.1 \text{ s}$	1.4	1.8

Table I. Comparison of the detection efficiencies of MLy and cWB at a FAR of 1/year. The first column is the label used for each waveform in Figure 9. The second column indicates the signal polarisation: L (linear: $h_{\times} = 0$), E (elliptical: $|h_{\times}| \leq |h_{+}|$), or U (unpolarised: $|h_{\times}| = |h_{+}|$). The third column lists the waveform parameters; see [60] for definitions. The two rightmost columns are the h_{rss} values in units of $10^{-22} \text{ Hz}^{-1/2}$ at which the MLy and cWB pipelines achieve 50% detection efficiency for each waveform type. A ‘–’ indicates no data available for cWB for that waveform.

to estimate accurately the threshold for FAR values of $O(1/\text{year})$ with days to weeks of data; three or four A100-SXM4 GPUs will therefore be sufficient to perform the full analysis while keeping up with the data in real time. This is in contrast to the several hundred dedicated CPUs typically required by standard algorithms.

Finally, we note that the computational cost of training is modest. A single training of one model on a Tesla V100-SXM2-16GB GPU takes ~ 1 hour, and training both models 7 times each takes ~ 12 hours.

V. CONCLUSIONS AND FUTURE WORK

We have presented a novel CNN-based analysis pipeline, MLy, for the detection of transient gravitational-wave signals. Unlike previous CNN-based analyses, MLy is capable of detecting waveforms with morphologies that are not included in the training set while rejecting real detector noise glitches. The analysis is shown to be sensitive to a variety of waveform morphologies at signal-to-noise ratios and false alarm rates relevant for issuing rapid alerts to the astronomical community, with very low computing requirements and second-scale latencies possible. We propose MLy for low-latency running in the upcoming fourth LIGO-Virgo-KAGRA observing run [72].

The MLy pipeline uses a multi-component architecture in which one CNN detects transients that are simultaneous in multiple detectors while a second detects correlation between the detectors to eliminate coincident background glitches. The second CNN takes as input both the whitened detector timeseries data and the Pearson correlation between detectors computed for all physically allowed light travel time delays between detectors, allowing the CNN to detect signal correlation rather than signal shape. We suggest that using separate models to identify different aspects or properties of the desired signal may be a useful approach generally for GW analysis with machine learning methods.

While our model already has sensitivity approaching that of standard low-latency analyses, we consider this investigation to be a promising first attempt with potential for improvement. For example, we could use knowledge of the morphology of common glitch types to reduce the background. Our training used simulated glitches with the same morphology as the simulated GWBs to force our models to recognise GWBs by coincidence and correlation between detectors rather than by signal morphology, since the morphology of real GWBs is not known. However, the morphology of real glitches *is* known. Examination of the noise events in the non-Gaussian tail of the background distribution of Figure 6 shows that many of them are due to known glitch types recognised by Gravity Spy [56, 57, 86, 87]. Applying a glitch classifier or an auto-encoder to candidate events detected by MLy may allow us to identify false alarms as glitches and thereby veto them. Another improvement might be to boost the sensitivity to linearly polarised signals such as those produced by cosmic string cusps by training using a variety of signal polarisations.

While we have demonstrated MLy’s ability to detect GWBs, the characterisation of any detected signals (commonly referred to “parameter estimation”) is an open problem for unmodelled GWBs, and is necessary for the full exploitation of any detections. Existing machine-learning based methods [23, 27, 28, 45–47] (see also [88]) are fast but rely on precise signal models for training. By contrast the BAYESWAVE algorithm [65] is applicable to generic GWBs, estimating the waveform and providing a map of the probability distribution of the source over the sky, but typically requires hours to run for a single event. Given our goal of using MLy for the low-latency detection of GWBs to allow electromagnetic follow-up observations, a natural next step is to explore how sky-localisation pipelines such as [45] can be generalised to the case of unmodelled GWBs. We leave examination of this topic to a future work.

ACKNOWLEDGMENTS

We thank Erik Katsavounidis for helpful comments on an earlier draft. We thank Shubhanshu Tiwari for providing the sensitivity estimates for cWB listed in

Table I. We thank the LIGO Scientific Collaboration for access to computing resources for this work. This

work was supported by STFC grants ST/N005430/1 and ST/V005618/1.

-
- [1] J. A. et al., *Classical and Quantum Gravity* **32**, 074001 (2015).
- [2] F. A. et al., *Classical and Quantum Gravity* **32**, 024001 (2014).
- [3] B. Abbott, R. Abbott, T. Abbott, *et al.* (LIGO Scientific Collaboration and Virgo Collaboration), *Physical Review X* **9** (2019), 10.1103/physrevx.9.031040.
- [4] B. P. Abbott, R. Abbott, T. D. Abbott, *et al.* (LIGO Scientific Collaboration and Virgo Collaboration), *The Astrophysical Journal* **892**, L3 (2020).
- [5] R. Abbott, T. Abbott, S. Abraham, *et al.* (LIGO Scientific Collaboration and Virgo Collaboration), *Physical Review D* **102** (2020), 10.1103/physrevd.102.043015.
- [6] R. Abbott, T. D. Abbott, S. Abraham, *et al.*, *The Astrophysical Journal* **896**, L44 (2020).
- [7] R. Abbott, T. D. Abbott, S. Abraham, *et al.* (LIGO Scientific Collaboration and Virgo Collaboration), *Phys. Rev. Lett.* **125**, 101102 (2020).
- [8] <https://gracedb.ligo.org/superevents/public/O3/>.
- [9] T. L. S. Collaboration, the Virgo Collaboration, and the KAGRA Collaboration, “Gwtc-3: Compact binary coalescences observed by ligo and virgo during the second part of the third observing run,” (2021), [arXiv:2111.03606 \[gr-qc\]](https://arxiv.org/abs/2111.03606).
- [10] B. P. Abbott, R. Abbott, T. D. Abbott, *et al.* (LIGO Scientific Collaboration and Virgo Collaboration), *Phys. Rev. Lett.* **116**, 061102 (2016).
- [11] B. P. Abbott, R. Abbott, T. D. Abbott, *et al.* (LIGO Scientific Collaboration and Virgo Collaboration), *The Astrophysical Journal Letters* **848**:L12, 59 (2017), [arXiv:1710.05833 \[astro-ph.HE\]](https://arxiv.org/abs/1710.05833).
- [12] K. Kyutoku, S. Fujibayashi, K. Hayashi, K. Kawaguchi, K. Kiuchi, M. Shibata, and M. Tanaka, *Astrophys. J.* **890**, L4 (2020), [arXiv:2001.04474 \[astro-ph.HE\]](https://arxiv.org/abs/2001.04474).
- [13] B. P. Abbott, R. Abbott, T. D. Abbott, *et al.* (LIGO Scientific Collaboration and Virgo Collaboration), *Phys. Rev. Lett.* **119**, 161101 (2017).
- [14] D. Kasen, B. Metzger, J. Barnes, E. Quataert, and E. Ramirez-Ruiz, *Nature* **551**, 80 (2017).
- [15] B. P. Abbott, R. Abbott, T. D. Abbott, *et al.* (LIGO Scientific Collaboration and Virgo Collaboration), *Phys. Rev. Lett.* **121**, 161101 (2018).
- [16] B. P. Abbott, R. Abbott, T. D. Abbott, *et al.* (LIGO Scientific Collaboration and Virgo Collaboration), *The Astrophysical Journal* **850**, L39 (2017).
- [17] B. P. Abbott, R. Abbott, T. D. Abbott, *et al.* (LIGO Scientific Collaboration and Virgo Collaboration), *Nature* **551**, 85 (2017).
- [18] B. P. Abbott, R. Abbott, T. D. Abbott, *et al.* (LIGO Scientific Collaboration and Virgo Collaboration), *The Astrophysical Journal* **875**, 161 (2019).
- [19] D. George and E. A. Huerta, *Physical Review D* **97**, 044039 (2017), [arXiv: 1701.00008](https://arxiv.org/abs/1701.00008).
- [20] H. Gabbard, M. Williams, F. Hayes, and C. Messenger, *Physical Review Letters* **120**, 141103 (2018), [arXiv: 1712.06041](https://arxiv.org/abs/1712.06041).
- [21] C. Bresten and J.-H. Jung, [arXiv:1910.08245 \[astro-ph, physics:gr-qc, physics:physics\]](https://arxiv.org/abs/1910.08245) (2019), [arXiv: 1910.08245](https://arxiv.org/abs/1910.08245).
- [22] H. Wang, Z. Cao, X. Liu, S. Wu, and J.-Y. Zhu, [arXiv:1909.13442 \[astro-ph, physics:gr-qc\]](https://arxiv.org/abs/1909.13442) (2019), [arXiv: 1909.13442](https://arxiv.org/abs/1909.13442).
- [23] D. George and E. A. Huerta, [arXiv:1711.07966 \[astro-ph, physics:gr-qc\]](https://arxiv.org/abs/1711.07966) (2017), [arXiv: 1711.07966](https://arxiv.org/abs/1711.07966).
- [24] A. Schmitt, K. Fu, S. Fan, and Y. Luo, in *Proceedings of the 2nd International Conference on Computer Science and Software Engineering*, CSSE 2019 (Association for Computing Machinery, New York, NY, USA, 2019) p. 73–78.
- [25] T. D. Gebhard, N. Kilbertus, I. Harry, and B. Schölkopf, *Physical Review D* **100**, 063015 (2019), [arXiv: 1904.08693](https://arxiv.org/abs/1904.08693).
- [26] H.-M. Luo, W. Lin, Z.-C. Chen, and Q.-G. Huang, *Frontiers of Physics* **15**, 14601 (2019).
- [27] X. Fan, J. Li, X. Li, Y. Zhong, and J. Cao, *Science China Physics, Mechanics & Astronomy* **62**, 969512 (2019).
- [28] C. Chatterjee, L. Wen, F. Diakogiannis, and K. Vinsen, “Extraction of binary black hole gravitational wave signals from detector data using deep learning,” (2021), [arXiv:2105.03073 \[gr-qc\]](https://arxiv.org/abs/2105.03073).
- [29] D. S. Deighan, S. E. Field, C. D. Capano, and G. Khanna, *Neural Computing and Applications* (2021), 10.1007/s00521-021-06024-4.
- [30] E. A. Huerta and Z. Zhao, *Handbook of Gravitational Wave Astronomy*, 1–27 (2021).
- [31] W. Wei, A. Khan, E. Huerta, X. Huang, and M. Tian, *Physics Letters B* **812**, 136029 (2021).
- [32] W. Wei and E. Huerta, *Physics Letters B* **816**, 136185 (2021).
- [33] M. L. Chan, I. S. Heng, and C. Messenger, *Phys. Rev. D* **102**, 043022 (2020).
- [34] A. Iess, E. Cuoco, F. Morawski, and J. Powell, “Core-collapse supernova gravitational-wave search and deep learning classification,” (2020), [arXiv:2001.00279 \[gr-qc\]](https://arxiv.org/abs/2001.00279).
- [35] P. Astone, P. Cerdá-Durán, I. Di Palma, M. Drago, F. Muciaccia, C. Palomba, and F. Ricci, *Phys. Rev. D* **98**, 122002 (2018).
- [36] M. López, I. Di Palma, M. Drago, P. Cerdá-Durán, and F. Ricci, *Phys. Rev. D* **103**, 063011 (2021).
- [37] A. W. Steiner, S. Gandolfi, F. J. Fattoyev, and W. G. Newton, *Phys. Rev. C* **91**, 015804 (2015), [arXiv:1403.7546 \[nucl-th\]](https://arxiv.org/abs/1403.7546).
- [38] B. P. Abbott, R. Abbott, Abbott, and et al., *Physical Review Letters* **121** (2018), 10.1103/physrevlett.121.161101.
- [39] A. L. Piro and E. Pfahl, *The Astrophysical Journal* **658**, 1173 (2007).
- [40] M. H. P. M. van Putten, *The Astrophysical Journal* **684**, L91 (2008).
- [41] M. H. P. M. van Putten, N. Kanda, H. Tagoshi, D. Tatum, F. Masa-Katsu, and M. Della Valle, *Phys. Rev. D* **83**, 044046 (2011).

- [42] H. Shen, D. George, E. A. Huerta, and Z. Zhao, (2017), [arXiv: 1711.09919](#).
- [43] E. A. Huerta and Z. Zhao, “Advances in machine and deep learning for modeling and real-time detection of multi-messenger sources,” in *Handbook of Gravitational Wave Astronomy*, edited by C. Bambi, S. Katsanevas, and K. D. Kokkotas (Springer Singapore, Singapore, 2020) pp. 1–27.
- [44] E. Cuoco *et al.*, *Mach. Learn. Sci. Tech.* **2**, 011002 (2021), [arXiv:2005.03745 \[astro-ph.HE\]](#).
- [45] C. Chatterjee, L. Wen, K. Vinsen, M. Kovalam, and A. Datta, *Physical Review D* **100** (2019), [10.1103/physrevd.100.103025](#).
- [46] H. Shen, E. A. Huerta, Z. Zhao, E. Jennings, and H. Sharma, [arXiv:1903.01998 \[astro-ph, physics:gr-qc, stat\]](#) (2019), [arXiv: 1903.01998](#).
- [47] H. Gabbard, C. Messenger, I. S. Heng, F. Tonolini, and R. Murray-Smith, *Nature Phys.* **18**, 112 (2022), [arXiv:1909.06296 \[astro-ph.IM\]](#).
- [48] S. Khan and R. Green, *Physical Review D* **103** (2021), [10.1103/physrevd.103.064015](#).
- [49] W. Wei and E. Huerta, *Physics Letters B* **800**, 135081 (2020).
- [50] L. Blanchet, *Living Reviews in Relativity* **17** (2014), [10.12942/lrr-2014-2](#).
- [51] K. He, X. Zhang, S. Ren, and J. Sun, in *2016 IEEE Conference on Computer Vision and Pattern Recognition (CVPR)* (2016) pp. 770–778.
- [52] C. D. Ott, *Classical and Quantum Gravity* **26**, 063001 (2009).
- [53] E. Abdikamalov, G. Pagliaroli, and D. Radice, “Gravitational waves from core-collapse supernovae,” in *Handbook of Gravitational Wave Astronomy*, edited by C. Bambi, S. Katsanevas, and K. D. Kokkotas (Springer Singapore, Singapore, 2020) pp. 1–37.
- [54] V. Skliris, M. R. K. Norman, and P. J. Sutton, (2020), [arXiv:2009.14611v1 \[astro-ph.IM\]](#).
- [55] T. Marianer, D. Poznanski, and J. X. Prochaska, *Monthly Notices of the Royal Astronomical Society* **500**, 5408 (2020), [https://academic.oup.com/mnras/article-pdf/500/4/5408/34925881/staa3550.pdf](#).
- [56] M. Zevin, S. Coughlin, S. Bahaadini, E. Besler, N. Rohani, S. Allen, M. Cabero, K. Crowston, A. K. Katsaggelos, S. L. Larson, T. K. Lee, C. Lintott, T. B. Littenberg, A. Lundgren, C. Østerlund, J. R. Smith, L. Trouille, and V. Kalogera, *Classical and Quantum Gravity* **34**, 064003 (2017).
- [57] S. Bahaadini, V. Noroozi, N. Rohani, S. Coughlin, M. Zevin, J. Smith, V. Kalogera, and A. Katsaggelos, *Information Sciences* **444**, 172 (2018).
- [58] S. Klimenko *et al.*, *Phys. Rev. D* **93**, 042004 (2016), [arXiv:1511.05999 \[gr-qc\]](#).
- [59] B. P. Abbott, R. Abbott, T. D. Abbott, *et al.* (LIGO Scientific Collaboration and Virgo Collaboration), *Phys. Rev. D* **95**, 042003 (2017).
- [60] B. Abbott, R. Abbott, T. Abbott, S. Abraham, F. Acernese, K. Ackley, C. Adams, R. Adhikari, V. Adya, C. Affeldt, and *et al.*, *Physical Review D* **100** (2019), [10.1103/physrevd.100.024017](#).
- [61] B. P. Abbott, R. Abbott, T. D. Abbott, *et al.* (LIGO Scientific Collaboration and Virgo Collaboration), *Classical and Quantum Gravity* **33**, 134001 (2016).
- [62] S. Klimenko, G. Vedovato, V. Nacula, F. Salemi, M. Drago, E. Chassande-Mottin, V. Tiwari, C. Lazzaro, B. O’Brian, M. Szczepanczyk, S. Tiwari, and V. Gayathri, (2020).
- [63] R. Lynch, S. Vitale, R. Essick, E. Katsavounidis, and F. Robinet, *Phys. Rev. D* **95**, 104046 (2017).
- [64] P. J. Sutton, G. Jones, S. Chatterji, P. Kalmus, I. Leonor, S. Poprocki, J. Rollins, A. Searle, L. Stein, M. Tinto, and M. Was, *New Journal of Physics* **12**, 053034 (2010).
- [65] N. J. Cornish and T. B. Littenberg, *Classical and Quantum Gravity* **32**, 135012 (2015).
- [66] H. Ismail Fawaz, G. Forestier, J. Weber, L. Idoumghar, and P.-A. Muller, *Data Mining and Knowledge Discovery* **33**, 917–963 (2019).
- [67] L. N. Smith, “Cyclical learning rates for training neural networks,” (2017), [arXiv:1506.01186 \[cs.CV\]](#).
- [68] L. Cadonati, *Classical and Quantum Gravity* **21**, S1695–S1703 (2004).
- [69] L. Cadonati and S. Márka, *Classical and Quantum Gravity* **22**, S1159 (2005).
- [70] S. Chatterji, A. Lazzarini, L. Stein, P. J. Sutton, A. Searle, and M. Tinto, *Phys. Rev. D* **74**, 082005 (2006).
- [71] [https://www.gw-openscience.org/](#).
- [72] B. P. Abbott, R. Abbott, T. D. Abbott, *et al.* (LIGO Scientific Collaboration and Virgo Collaboration and KAGRA Collaboration), *Living Rev. Relativ* **21** (2013), [arXiv:1304.0670 \[gr-qc\]](#).
- [73] J. W. Murphy, C. D. Ott, and A. Burrows, *The Astrophysical Journal* **707**, 1173 (2009).
- [74] T. Damour and A. Vilenkin, *Phys. Rev. Lett.* **85**, 3761 (2000).
- [75] V. Skliris, “MLy, gravitational waves and machine learning library,” [https://git.ligo.org/vasileios.skliris/mly](#).
- [76] A. Nitz, I. Harry, D. Brown, C. M. Biwer, J. Willis, T. D. Canton, *et al.*, “*gwastro/pycbc: Pycbc release v1.16.9*,” (2020).
- [77] D. Macleod, A. L. Urban, S. Coughlin, T. Massinger, M. Pitkin, R. George, Paulalain, J. Areeda, L. Singer, E. Quintero, K. Leinweber, and T. G. Badger, “*gwpy/gwpy: 2.0.1*,” (2020).
- [78] F. Chollet *et al.*, “*Keras*,” (2015).
- [79] [https://git.ligo.org/vasileios.skliris/detecting-unmodeled-gravitational-wave-transients-using-convolutional-neural-networks](#).
- [80] [https://emfollow.docs.ligo.org/userguide/analysis/index.html](#).
- [81] Müller, E., Janka, H.-Th., and Wongwathanarat, A., *A&A* **537**, A63 (2012).
- [82] T. Damour and A. Vilenkin, *Phys. Rev. D* **64**, 064008 (2001).
- [83] S. Husa, S. Khan, M. Hannam, M. Pürrer, F. Ohme, X. J. Forteza, and A. Bohé, *Phys. Rev. D* **93**, 044006 (2016).
- [84] S. Khan, S. Husa, M. Hannam, F. Ohme, M. Pürrer, X. J. Forteza, and A. Bohé, *Phys. Rev. D* **93**, 044007 (2016).
- [85] S. Tiwari, private communication.
- [86] S. B. Coughlin, S. Bahaadini, N. Rohani, M. Zevin, O. Patane, M. Harandi, C. Jackson, V. Noroozi, S. Allen, J. Areeda, M. W. Coughlin, P. Ruiz, C. P. L. Berry, K. Crowston, A. K. Katsaggelos, A. Lundgren, C. Osterlund, J. R. Smith, L. Trouille, and V. Kalogera, *Physical Review D* **99**, 082002 (2019), [arXiv: 1903.04058](#).
- [87] S. Soni *et al.*, *Class. Quant. Grav.* **38**, 195016 (2021), [arXiv:2103.12104 \[gr-qc\]](#).

- [88] L. P. Singer and L. R. Price, [Physical Review D](#) **93** (2016), [10.1103/physrevd.93.024013](#).